Inorganic Chemistry
Cite This: Inorg. Chem. 2019, 58, 5900−5913
Article
pubs.acs.org/IC

α-$AgVO_3$ Decorated by Hydroxyapatite ($Ca_{10}(PO_4)_6(OH)_2$): Tuning Its Photoluminescence Emissions and Bactericidal Activity

Jussara Soares da Silva,[†] Thales R. Machado,[†] Tiago A. Martins,[†] Marcelo Assis,[†] Camila C. Foggi,[†] Nadia G. Macedo,[†] Héctor Beltrán-Mir,[‡] Eloisa Cordoncillo,[‡] Juan Andrés,[§] and Elson Longo*,[†]

[†]Departamento de Química, CDMF, Universidade Federal de São Carlos (UFSCar), 13565-905São Carlos, São Paulo, Brazil
[‡]Departament de Química Inorgànica i Orgànica, Universitat Jaume I (UJI), 12071 Castellón de la Plana, Castelló, Spain
[§]Departament de Química Física i Analítica, Universitat Jaume I (UJI), 12071 Castellón de la Plana, Castelló, Spain

Supporting Information

ABSTRACT: Defect-related luminescent materials have attracted interest because of their excellent optical properties and are considered as a less expensive and nontoxic alternative to commonly used lanthanide-based optical systems. These materials are fundamentally and technologically important for the next generation of full-color tunable light-emitting diodes as well as in the biomedical field. In this study, we report the preparation of α-silver vanadate (α-$AgVO_3$, AV) decorated by hydroxyapatite ($Ca_{10}(PO_4)_6(OH)_2$, HA) with intense photoluminescence (PL) emissions at various HA/AV molar ratios (1:1−1:1/32) by a simple route based on chemical precipitation. The well-defined diffraction peaks observed by X-ray diffraction were all indexed to the monoclinic AV and hexagonal HA phases. Analysis of the results obtained by Fourier transform infrared spectroscopy reveals the presence of short-range structural order as deduced by the characteristic vibrational modes assigned to AV and HA systems. Characterization by scanning and transmission electron microscopies confirms the presence of AV and HA micro- and nanorods, respectively. UV−vis spectroscopy renders band gap energies of 5.80 eV for HA and in the range 2.59−2.65 eV for pure AV and HA/AV samples. The PL data reveal the presence of broad-band emission profiles, typical of defect-related optical centers in materials. Depending on the molar ratio, the emission can be completely tunable from the blue to red spectral regions; in addition, pure white color emission was obtained. On the basis of these results, we propose an order−disorder model induced by structural and interface defects to explain the PL emissions in the HA/AV system. Moreover, our results show that HA/AV composites have superior bactericidal activity against *Staphylococcus aureus* (methicillin-resistant and methicillin-susceptible) and can be used as a novel multifunctional material.

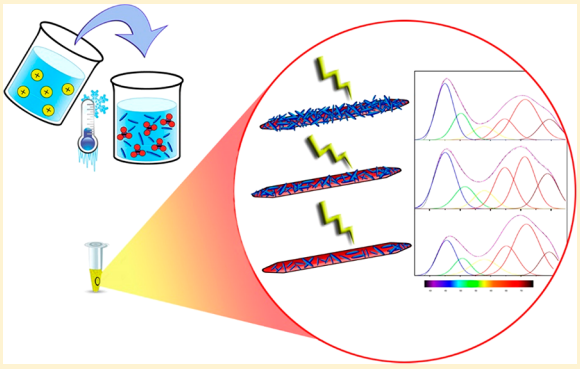

■ INTRODUCTION

Today, energy used for lighting corresponds to 20% of global energy consumption.[1] Thus, developing new efficient technologies for lighting is a matter of worldwide urgency. Among the devices available, solid-state lighting (SSL) sources based on semiconductors, including light-emitting diodes (LEDs) and white-light LEDs (WLEDs), have been extensively applied for general illumination as well as in many other fields, e.g., automotive lighting, automobile devices, display backlighting, communication devices/networks, and medical applications.[2−4] This is due to the many advantages related to these systems when compared with conventional light sources, such as high efficiency, low power consumption, high reliability, long lifetime, and environment friendliness.[5] However, a current challenge is the design of highly efficient optical materials without the need for activator ions comprised of lanthanides such as Eu^{2+}, Eu^{3+}, Ce^{3+}, Yb^{3+}, and Tb^{3+}, because of the high cost and environmental impact associated with their extraction and purification processes.[6]

White-light materials can be generated by various methods, including the accommodation of single or multiple lanthanides in a host lattice with low optical activity, by co-doping ion pairs based on an energy transfer mechanism, and self-activated luminescent materials activated by structural, surface, and interface defects.[7,8] This latter mechanism is quite interesting since intense, stable, and tunable emissions can be achieved without the necessity of dopants. Moreover, a great variety of emission colors can be obtained with these systems since the luminescence response of distinct materials or in the same material depends upon the concentration and nature of defects, which can be controlled by the experimental conditions employed for their preparation and processing.[9−13]

Hydroxyapatite, ($Ca_{10}(PO_4)_6(OH)_2$, HA) is a biomaterial with superior biocompatibility and bioactivity due to its similarities with the mineral phase of bones and teeth

Received: January 25, 2019
Published: April 23, 2019

DOI: 10.1021/acs.inorgchem.9b00249
Inorg. Chem. 2019, 58, 5900−5913

(bioapatite) and is considered ideal for biomedical approaches.[14] One of the most important structural features of HA for a wide range of applications is its unique ability to accept lattice distortions. Synthetic and natural HA crystallizes in almost all cases in the hexagonal $P6_3/m$ space group symmetry, which is stabilized by foreign ion inclusion and vacancy formation, and the defect-free monoclinic $P2_1/b$ phase rarely occurs.[15] Hence, HA can stabilize half of all the elements of the periodic table in each of its crystalline sites as well as defects, vacancies, and byproducts of synthesis reactions, in almost any valence state and with large differences in ionic radii, without breaking its crystal symmetry.[16] Recently, various studies demonstrated that it is possible to take advantage of this peculiarity of synthetic HA nanoparticles obtained by low-temperature pathways for the stabilization of efficient blue (λ_{em} = 395−420 nm) defective luminescent centers.[17−19] Our research group is engaged in the study of intrinsic photoluminescence (PL) emissions of HA and how to control the color of the emission from blue to yellow (λ_{em} = 440−610 nm) by varying the synthesis and heat treatment conditions.[20,21] Hence, the intense and broad-band emissions generated by HA nanoparticles can be successfully used in optical devices and biomedical approaches without the necessity of activator dopants such as lanthanide elements.[22−26]

On the other hand, silver vanadate ($AgVO_3$, AV) has attracted interest for biomedical and electrochromic devices, bactericidal agents, and other applications.[27,28] However, the optical properties of these materials have not been greatly studied in the literature.[29,30] There are four distinct crystalline phases for this material: α-$AgVO_3$, β-$AgVO_3$, δ-$AgVO_3$, and γ-$AgVO_3$.[31,32] In a recent study, our research group studied the α- and β-AV polymorphs as photoluminescent materials[33] and the electronic structure, morphology, optical features, and bactericidal activity of α-AV.[30] This latter study points out that α-AV presents structural and surface defects which lead to an intense broad-band emission in the red region of the electromagnetic spectrum, where these emissions are derived from multiphoton processes between defect energy levels.

The combination of two or more materials is of wide scientific research interest because this can combine the properties of single materials and generally present unique properties by synergistic effects.[34] Our research group demonstrated that the combination of inorganic materials with intense defect-related luminescence is a promising strategy to obtain tunable emission colors.[35,36] In particular, among the distinct strategies for tuning the spectral range of PL emissions of HA and AV materials separately (generally blue for HA and red for AV), we can list the synthesis and heat treatment conditions, incorporation of lattice impurities, and order−disorder effects. However, to the best of the authors' knowledge, there are no reports in the literature of their combination to improve the overall PL properties of AV decorated by HA.

Herein, the objectives of the present study are 3-fold. First, we report the facile synthesis of α-AV samples decorated by HA (HA/AV); second, we investigate in detail how the molar ratio between HA and AV controls the structural ordering at long and short range, morphological features, and the tunable PL emissions from intense blue to red emission colors as well as white-light emission; finally, we demonstrate the enhanced bactericidal activity of HA/AV samples.

■ EXPERIMENTAL SECTION

Synthesis of HA Nanorods. HA nanoparticles were synthesized by chemical precipitation in accordance with our previous studies.[20,21] Briefly, 10 mmol of calcium nitrate tetrahydrate ($Ca(NO_3)_2{\cdot}4H_2O$; 99.0%, Sigma-Aldrich; CAS Reg. No. 13477-34-4) were dissolved in 50 mL of Milli-Q water. In another flask, 6 mmol of diammonium phosphate ($(NH_4)_2HPO_4$; 98.0%, Strem Chemicals; CAS Reg. No. 7783-28-0) was dissolved in 100 mL of Milli-Q water. The pH values of the two solutions were adjusted to 9.5−10.0 with NH_4OH, and the solutions were heated to 90 °C and subsequently mixed, by dripping the entire phosphate precursor solution onto the calcium precursor solution by flow peristaltic pumping at 7.00 mL/min. After precipitation the solution was maintained at 90 °C with stirring for 2 h and the pH of the supernatant was maintained in the range 9.5−10.0 with ammonia. Then, the precipitate formed was centrifuged and washed several times with Milli-Q water and ethanol and was dried at 80 °C in the oven for 24 h.

Synthesis of Pure AV Microrods. The AV powder was synthesized as adapted from a previous publication.[30] Initially 0.2 mmol of ammonium metavanadate (NH_4VO_3; 99.0%, Sigma-Aldrich; CAS Reg. No. 7803-55-6) was dissolved in 5.86 mL of distilled water by magnetic stirring and heated to complete solubilization. Then 0.2 mmol of silver nitrate ($AgNO_3$; 99.8%, Cennabras; CAS Reg. No. 7761-88-8) was solubilized in 5.86 mL of distilled water until the solution became clear. Both solutions were cooled to approximately 10 °C and mixed with immediate release of the silver precursor onto the vanadate precursor, and instant formation of AV preciptate (orange supernatant and yellowish precipitate). The mixture was rapidly centrifuged, and the precipitate was washed several times with distilled water and finally dried at 70 °C in the oven for 24 h.

Precipitation of HA-Decorated AV Samples. The HA/AV samples were prepared by a chemical precipitation of AV microrods in a solution containing dispersed HA nanoparticles. For this pathway, 200 μmol of NH_4VO_3 was dissolved in 5.86 mL of distilled water by magnetic stirring and heated to complete solubilization. In this solution, 200 μmol of the HA sample obtained as described above in Synthesis of HA Nanorods was dispersed by ultrasonic shaking performed for 15 min. In another flask, 200 μmol of $AgNO_3$ was dissolved in 5.86 mL of distilled water until the solution became clear. Then both solutions were cooled to approximately 10 °C. Subsequently, the solutions were quickly mixed by adding the silver precursor into the vanadate precursor containing the HA nanoparticles in an ultrasound bath. This procedure yielded yellowish suspended particles which were allowed to settle. The resulting precipitate was washed several times with distilled water and finally dried at 70 °C in the oven for 24 h. The sample obtained is referred to as the HA/AV 1 sample.

Preparation of the other HA/AV samples followed an experimental procedure similar to that for the HA/AV 1 sample. The only difference was the amount of HA nanorods dispersed in vanadate precursor solution. In these cases, 100, 50, 25, 12, and 6 μmol of the HA sample were dispersed, leading to the HA/AV 2, HA/AV 3, HA/AV 4, HA/AV 5, and HA/AV 6 samples, respectively. Table 1 lists the main experimental parameters used for each HA/AV sample studied.

Characterization. The obtained samples were characterized by X-ray diffraction (XRD) using a Rigaku-DMax/2500PC (Japan) diffractometer with Cu Kα radiation (λ = 1.5406 Å) in the 2θ range 10°−60° with a scanning speed of 0.2°/min. The peaks of the samples were indexed according to standards of the Joint Committee of Powder Diffraction Standards (JCPDS). Fourier transform infrared spectroscopy (FTIR) was performed at room temperature using a Jasco FT/IR-6200 (Japan) spectrophotometer operated in absorbance mode. The spectra have a resolution of 4 cm^{-1} and 32 accumulations per measurement in the range of 400−4000 cm^{-1}. These measurements were performed on 12 mm diameter pellets which were composed of 1% by weight of each sample mixed with 99% by weight of KBr (99%, Sigma-Aldrich). UV−vis spectroscopic measurements were performed by Cary 5G spectrometer (Varian, USA) in diffuse reflection mode. Standard samples for the reflectance measurements

DOI: 10.1021/acs.inorgchem.9b00249
Inorg. Chem. 2019, 58, 5900−5913

Table 1. Principal Experimental Parameters and the Samples Prepared in the Present Study by Chemical Precipitation[a]

sample label	HA (μmol)	AV (μmol)	HA/AV (molar ratio)
HA/AV 1	200	200	1:1
HA/AV 2	100	200	1/2:1
HA/AV 3	50	200	1/4:1
HA/AV 4	25	200	1/8:1
HA/AV 5	12	200	1/16:1
HA/AV 6	6	200	1/32:1

[a]HA, hydroxyapatite; AV, α-silver vanadate. Components used in experimental samples.

were SRS-80-010 and SRS-02-010 for white and black Labsphere standards,[37] respectively. The morphological characteristics of the obtained materials were examined using a scanning electron microscope (SEM) Inspect F50 (FEI, The Netherlands) adjusted to an acceleration voltage of 5 or 20 kV with a working distance of 3 mm. The samples were prepared by dispersing the powders in water and then depositing them on metal Si plates. Transmission electron microscopy (TEM) and high-resolution TEM (HR-TEM) were performed using a FEI Tecnai F20 (Netherlands) microscope operating at 200 kV. High-angle annular dark-field (HAADF) image and elemental mapping by energy-dispersive X-ray spectroscopy (EDS) were recorded in the scanning TEM (STEM) mode.

Photoluminescence Emissions and Bactericidal Properties. PL spectra were collected using a Monospec 27 Monochromator Jarrel (TermalJarrel Ash, USA) coupled to an R955 photomultiplier (Hamamatsu Photonics, Japan). The measurements were performed at room temperature with a krypton ion laser (Innova Coherente 200 K; λ = 350 nm) as the excitation source with a maximum output power of 500 mW. All deconvolutions were made using the software PeakFit (version 4.05), with the Voigt Area G/L function.

Bactericidal activity was investigated against Gram-positive bacterium, methicillin-resistant (MRSA) and susceptible *Staphylococcus aureus* (*S. aureus*) (MSSA). The antimicrobial activity of the microcrystals was evaluated by measurement of the minimum inhibitory and bactericidal concentrations (MICs and MBCs) for planktonic cells of the two reference strains from the American Type Culture Collection MRSA ATCC 33591 and MSSA ATCC 25923. The tests were performed according to the Clinical and Laboratory Standards Institute broth microdilution method (document M7-A7, 2006).

The standard strain of *S. aureus* was streaked onto Mueller−Hinton agar plates (Acumedia Manufacturers Inc., Baltimore, MD, USA) and incubated at 37 °C for 24−48 h. One loopful of fresh cells of each microorganism grown on the agar plates was transferred to tryptic soy broth (TSB; Acumedia Manufacturers, Inc. Baltimore, MD, USA). After the cells were incubated overnight in an orbital shaker (75 rpm) at 37 °C, the cells were harvested and washed two times with a phosphate-buffered saline (PBS; pH 7.2) solution and centrifuged at 5.000*g* for 5 min. Washed fungal cells were resuspended in the TSB, and the suspensions were spectrophotometrically standardized to a final concentration of 10^7 CFU/mL by adjusting the optical density of the suspensions.

The MICs and MBCs were determined by incubating the microorganisms on 96-well microtiter plates for 24 h at 37 °C, exposed to 2-fold serial dilutions of each of the microcrystal solutions (from 1000 to 0.061 μg/mL) in specific culture media. Positive controls were inoculated with microbial suspension but no microcrystals, while un-inoculated culture medium was used as the negative control. The MICs were defined as the lowest concentrations of each solution required for the complete inhibition of growth (no visible growth by visual inspection).

To determine the MBCs, aliquots from 10-fold serial dilutions (from 10^{-1} to 10^{-8}) of each well were removed and inoculated (25 μL) on Mueller−Hinton agar in duplicate. After the cells were incubated for 24−48 h at 37 °C, the colony-forming units per milliliter (CFU/mL) were calculated and log-transformed. The MBCs were defined as the lowest concentrations of each of the microcrystal solutions that resulted in no bacterial growth on plates. The assays were performed in triplicate on three separate occasions.

Reactive Oxygen Species Detection. The production of reactive oxygen species (ROS) was evaluated along the photodegradation process using specific scavenger agents. Ascorbic acid (AA; Alfa Aesar) and *tert*-butyl alcohol (TBA; Alfa Aesar) were respectively used as the superoxide radical ($O_2^{\bullet-}$) and hydroxyl radical ($OH^{\bullet}$) scavengers. In addition, ammonium oxalate (AO; Alfa Aesar) was used as the hole scavenger ($h^{\bullet}$). The experimental procedure was performed using 0.625 mmol of the sequestrant and 50 mg of the probed samples (HA, AV, and HA/AV 6), which were added in 50 mL of aqueous solutions (0.0163 mmol/L) of rhodamine B (RhB; 95%, Sigma-Aldrich). The samples were dispersed for 30 min in an ultrasound bath. Subsequently, the resulting suspensions were exposed to irradiation provided by six UV lamps (Light Source Inc. G15/T8 15W, USA) with vigorous stirring in a photocatalytic system maintained at 20 °C using a thermostatic bath. Aliquots of the solutions were collected after 1 h of exposure. Then, solids from the aliquots were separated by centrifugation. Variations in the absorption

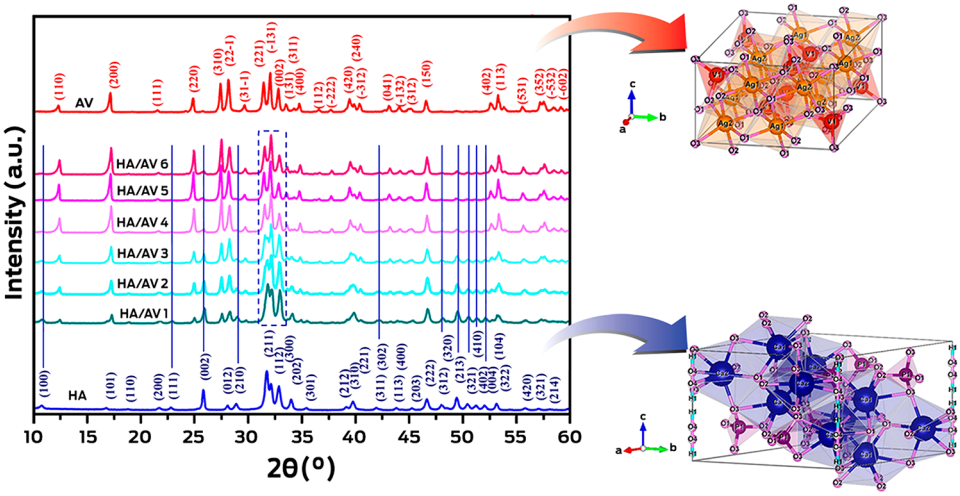

Figure 1. XRD patterns of pure HA and AV samples and HA-decorated AV samples. Schematic representations of the unit cells of AV and HA structures and coordination clusters for each element in these crystallographic arrangements are provided for clarity purposes.

DOI: 10.1021/acs.inorgchem.9b00249
Inorg. Chem. 2019, 58, 5900−5913

band maximum of RhB at λ = 553 nm were monitored by using a V-660 UV−vis spectrophotometer (Jasco, Japan).

RESULTS AND DISCUSSION

XRD Analysis. The crystalline phases as well the long-range structural order of all studied samples were characterized by XRD, and Figure 1 shows the diffraction patterns obtained. The peaks of the pure HA sample can all be perfectly indexed to its hexagonal phase with space group $P6_3/m$, in good agreement with the results reported in PDF No. 09-0432. This phase is built by tetrahedral $[PO_4]$ clusters arranged in a hexagonal compact packaging (ABABA) and has its crystal lattice modified by the Ca species inserted in the larger cavities of this arrangement. The 10 Ca species contained in the HA structure are arranged in two distinct sites. As also illustrated by Figure 1, the Ca(1) site results in clusters of $[CaO_9]$, in which the Ca cation is surrounded by nine O anions belonging to the PO_4 tetrahedra, and thus forms the columns in the ternary axes of the structure. The Ca(2) site results in clusters of $[CaO_7H]$, in which the Ca cation is surrounded by six O anions that make up the $[PO_4]$ groups and one OH group, and thus forms the hexagonal channels of the structure.[21,38]

On the other hand, the peaks present in the AV sample can all be associated with the crystallization of the monoclinic AV structure with space group C_2/c, in agreement with PDF No. 89-4396. The AV has its crystalline network formed by $[VO_4]$ clusters in which the Ag cations are inserted into the cavities between the $[VO_4]$ clusters. Ag cations are coordinated with six oxygen anions to form octahedral $[AgO_6]$ clusters, but there are two types of octahedral $[AgO_6]$ units with highly distorted geometries, resulting in two types of O−Ag−O bonding angles (Figure 1).[30] Peaks of a deleterious phase were not observed in either case, confirming the success of the synthetic route in obtaining single-phased HA and AV materials. Moreover, the sharp and well-defined peaks indicate significant long-range structural order (crystallinity) in these samples. However, it is important to emphasize that both structures are not free of lattice distortions in O−Ca−O, O−P−O, O−Ag−O, and O−V−O bond angles and Ca−O, P−O, Ag−O, and V−O bond lengths of the corresponding clusters. The presence of defects such as ionic/interstitial vacancies and the presence of impurities (H_2O, CO_3^{2-}, and NH_4^+) are typically observed in syntheses at low temperature in aqueous solution.[30,39]

The XRD profiles of the HA-decorated AV samples are essentially the superimposition of the patterns for the two individual components. Thus, the precipitation of AV into a solution containing HA nanoparticles does not induce the crystallization of other vanadium- or phosphate-based phases. The main difference between each decorated sample is the relative intensity of HA and AV peaks; i.e., the intensity of the main HA peaks decreases at the same time as a decrease in the concentration of this phase (from HA/AV 1 to HA/AV 6 samples). At 30−35° the principal peaks of the two materials overlap (highlighted in dashed blue rectangles in Figure 1), and the major contribution for the observed profile in this region gradually transitions from HA peaks (HA/AV 1) to AV peaks (HA/AV 6). Peaks of HA which do not overlap with AV are marked with blue lines.

FTIR Analysis. The short-range order of the prepared samples was evaluated by vibrational spectroscopy. Figure 2 shows (a) the region from 3000 to 4000 cm^{-1}, (b) the region from 1300 to 1800 cm^{-1}, and (c) the region from 400 to 1300 cm^{-1}. These magnifications are displayed for better interpretation of the principal vibrational modes deriving from the AV and HA structures which occur in these three regions. For the entire FTIR spectra, see Figure S1 in the Supporting Information (SI). As the figure shows, in pure AV and HA samples only the typical bands reported in the literature for each individual material were observed. All observed modes of the AV and HA samples are summarized in Tables 2 and 3.

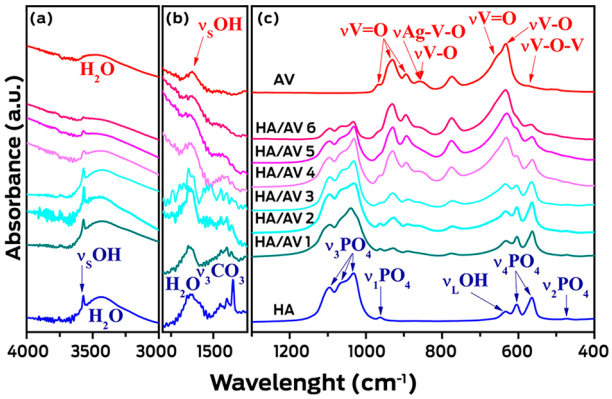

Figure 2. FTIR spectroscopy of the samples. Expanded regions in the following ranges: (a) 3000−4000, (b) 1300−1800, and (c) 400−1300 cm^{-1}.

Table 2. References of the Vibrational Modes from FTIR of HA

vibrational mode	Fowler et al.[40] (cm^{-1})	Markovic et al.[41] (cm^{-1})	this experiment (cm^{-1})
$\nu_2(PO_4)$	465/474	473	473
ν_4 PO_4	561/575/601	565/603	564/604
ν_L(OH)	630	669	633
$\nu_2(CO_3)$		872/874/880	873/885
$\nu_1(PO_4)$	962	960	963
$\nu_3(PO_4)$	1040/1092	1000−1150	1033/1065/1096
$\nu_3(CO_3)$		1418−1506	1415−1460
H_2O		1635/3000−3650	1637/3000−3600
ν_s(OH)	3572	3570	3573

Specifically, typical bands from HA chemically precipitated in an aqueous system can be identified, including the $[PO_4]$ bands at 473 cm^{-1} (ν_2), 564 and 604 cm^{-1} (v_4), 963 cm^{-1} (v_1), and 1033, 1065, and 1096 cm^{-1} (v_3).[40] Moreover, vibrational modes related to H_2O molecules occur at 1637 cm^{-1} and in

Table 3. References of the Vibrational Modes from FTIR of the Experimental AV According to the Literature

vibrational mode	Sivakumar et al.[44] (cm^{-1})	Andronache et al.[45] (cm^{-1})	Holtz et al.[46] (cm^{-1})	this experiment (cm^{-1})
ν_1(V−O−V)	511			508
δ(V−O)		633		633
ν(V=O)			677	654
polymeric vanadates			940−770	775
ν(V−O) and ν(Ag−O−V)			849	856
ν(V=O)			895	894
ν(V=O)			915	930
ν(V=O)			964	967
H_2O	1639/3432			1620/3500

DOI: 10.1021/acs.inorgchem.9b00249
Inorg. Chem. 2019, 58, 5900−5913

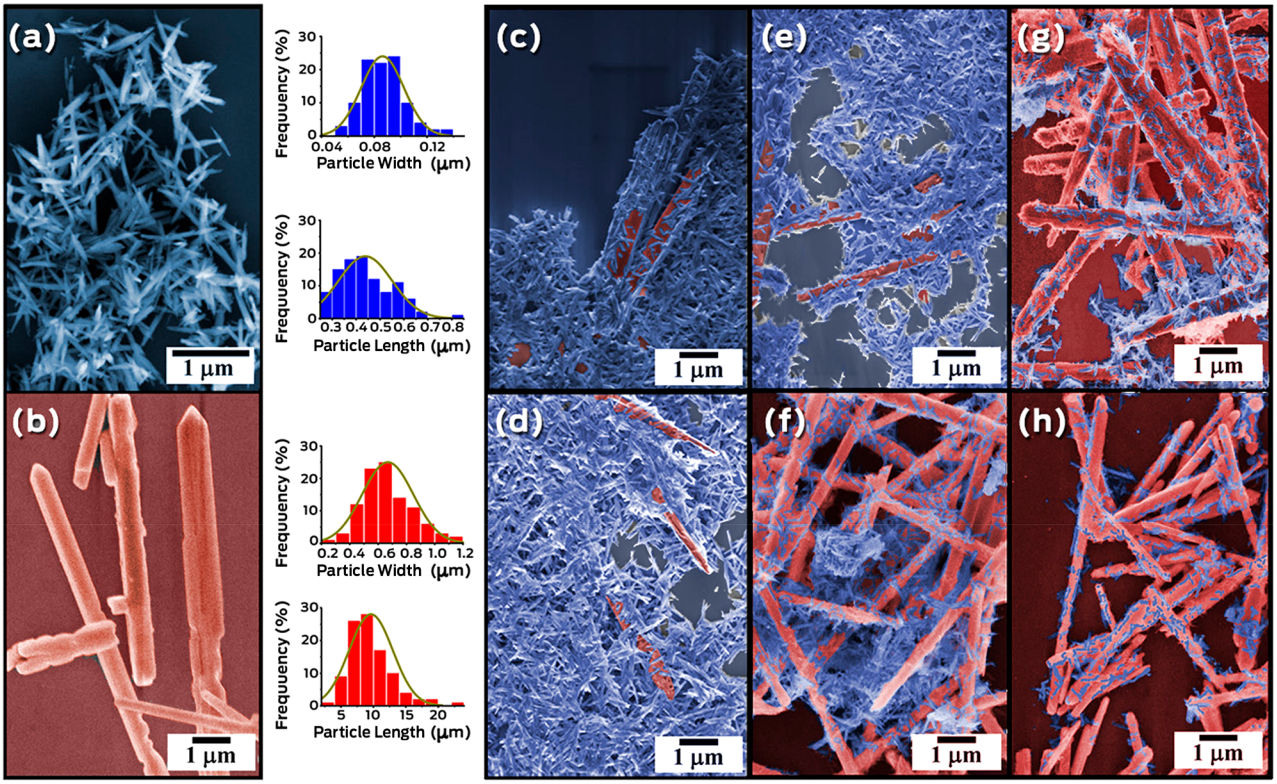

Figure 3. Morphological characterization of prepared samples obtained by FE-SEM technique. Micrographs for pure samples with their respective particle size estimations: (a) HA nanorods and (b) AV microrods. Micrographs for HA-decorated AV samples: (c) HA/AV 1, (d) HA/AV 2, (e) HA/AV 3, (f) HA/AV 4, (g) HA/AV 5, and (h) HA/AV 6.

the range 3000−3700 cm^{-1}. The stretching mode (ν_S) from the structural OH group of HA appears at 3573 cm^{-1} as a shoulder of the H_2O broad band, and the band at 633 cm^{-1} arises from the librational (ν_L) mode of the structural OH group.[39,40] Moreover, weak bands associated with structural CO_3^{2-} are also observed in the HA sample in the range 1415−1460 cm^{-1} and at 873 cm^{-1} (very weak, not shown).[41] CO_3^{2-} can substitute for PO_4^{3-} (B-type substitution) or for OH^- (A-type substitution) groups and, in this case, an AB-type substitution of carbonates at the HA sample can be detected. This substitution changes the properties of HA significantly, and in order to enable its occurrence, other charge compensation mechanisms are necessary, leading to extra vacancies (such as Ca and OH vacancies) and inclusion of impurities from the reaction medium (such as NH_4^+); these mechanisms cause deformations of the HA crystalline lattice.[42,43] This substitution process in an AB-type configuration in the HA structure is well-known in the synthetic procedure of HA obtained by chemical precipitation at aqueous solution.[41] On the other hand, in the pure AV sample, bands related to the VO_4 group, including ν(V−O−V) (508 cm^{-1}), δ(V−O) (633 cm^{-1}), and ν(V═O) (654, 894, 930, and 967 cm^{-1}) vibrational modes were observed, as well as bands at 775 cm^{-1} for polymeric vanadate groups, and 856 cm^{-1} for ν(V−O) and ν(Ag−O−V) stretching modes.[44−46] The bands at 1620 and 3500 cm^{-1} are associated with physisorbed water.[44] The vibrational modes were also confirmed in Raman spectroscopy for the pure samples (Figure S2). However, in the HA/AV decorated samples, the intensities of the Raman modes of the HA (Table S1) are masked by the high intensities of the modes from AV (Table S2), as also illustrated in Figure S2.

As in the case of XRD analysis, FTIR spectroscopy also proved to be a suitable technique to evaluate the decorated samples. The bands observed for HA-decorated AV samples correspond to the principal modes identified for the individual crystalline structures. No significant shifts in relation to the pure materials were sensed. The principal changes are related to the intensity of the AV and HA modes in proportion to their molar ratio, principally in the modes arising from phosphate, hydroxyl, and vanadate vibrations (Figure 2b). Thus, the quasi-linear and gradual decrease in intensity of HA bands from HA/AV 1 to HA/AV 6 samples confirms the successful obtention of AV samples decorated with distinct amounts of HA. Furthermore, the bandwidths can give information about the organization of the species comprising the structure of complex oxides and, specifically, the HA and AV samples.[21,30,47] In the present study, the AV, HA, and HA-decorated AV samples exhibit relatively well-defined FTIR bands, associated with the presence of short-range structural order.

FE-SEM and TEM Analyses. The morphological aspects of all prepared samples were first characterized by FE-SEM, and panels a−h of Figure 3 show the obtained micrographs. The pure HA and AV samples are composed of particles of similar shapes with a rod-like aspect (Figure 3a,b). The principal differences between them are their particle sizes. For a better interpretation, we measured the dimensions of 100 particles using distinct FE-SEM images collected from HA and AV pure samples. The pure HA sample is composed mainly of nanorods 0.09 μm in width and 0.45 μm in length. On the other hand, the particles of the pure AV sample are mainly microrods 0.7 μm in width and 10.0 μm in length. These results are consistent with previous literature reports of pure HA and AV particles precipitated in similar conditions.[21,30]

DOI: 10.1021/acs.inorgchem.9b00249
Inorg. Chem. 2019, 58, 5900−5913

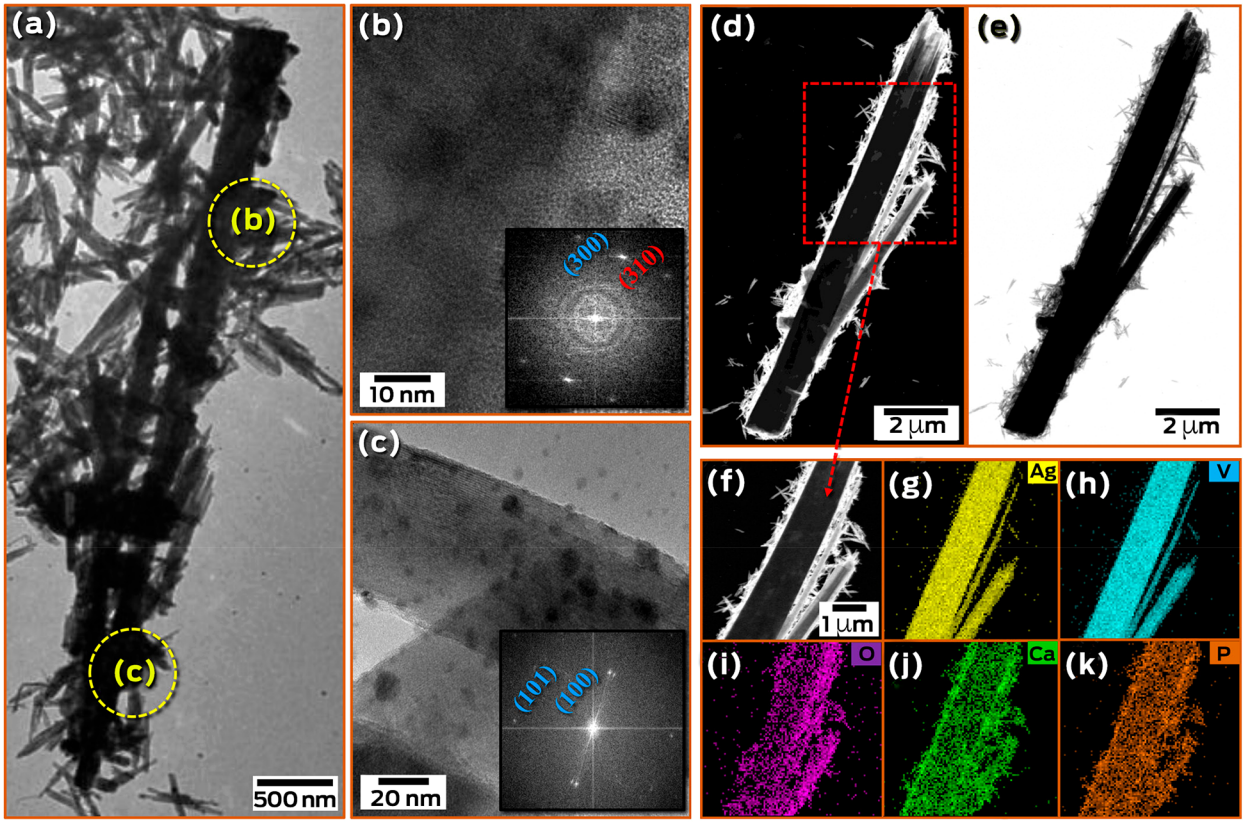

Figure 4. TEM characterization of HA-decorated AV. (a) Low magnification TEM micrograph showing the two regions studied by HR-TEM (regions b and c, yellow circles), (b) HR-TEM of region b and its FFT analysis (inset), and (c) HR-TEM of region c and its FFT analysis (inset). (d) Dark-field and (e) bright-field micrographs obtained in STEM mode. The red dotted square shows the specific region where elemental analysis by EDS mapping was conducted. (f) Magnified view of the EDS region and (g−k) the elemental distributions for Ag, V, O, Ca, and P, respectively. All analyses were performed in the HA/AV 3 sample.

Panels c−h of Figure 3 show the obtained micrographs for HA/AV samples. Essentially, the particle shapes of both HA and AV materials do not change significantly during the precipitation of AV into the aqueous solutions containing HA nanoparticles. As expected, the principal difference is the ratio of HA nanorods to AV microrods as the concentration of HA particles changes in the initial solution (from HA/AV 1 to HA/AV 6). Hence, in the three first samples with a high concentration of HA nanoparticles (HA/AV 1, HA/AV 2, and HA/AV 3), the HA concentrations used are enough to allow an almost homogeneous covering of the AV surface. In these cases, there is a slight excess of HA nanoparticles which are not in contact with AV surfaces and form some HA agglomerates. On the other hand, at lower concentrations of HA (samples HA/AV 4, HA/AV 5, and HA/AV 6), the HA nanorods partially cover the AV microrod surfaces; i.e., almost all HA nanoparticles are deposited on the surface of AV, but the concentration is not sufficient for complete coverage, and some AV surfaces are exposed.

Figure 4 shows the TEM characterization of the HA/AV 3 sample. In Figure 4a, an AV microrod covered by several HA nanorods can be seen. Two regions in this sample (labeled as regions b and c, yellow circles) were analyzed by HR-TEM images. Figure 4b shows the HR-TEM micrograph of region b associated with an interface between HA and AV particles. The fast fourier transform (FFT) of this region (inset) revealed the presence of reflections corresponding to (300) and (310) families of planes of hexagonal HA and monoclinic AV, respectively, in accordance with PDF No. 04-432 and PDF No. 89-4396, corroborating with XRD results. Figure 4c illustrates a region comprised of HA nanorods; the FFT of this region (inset) also revealed spots associated with the (100) and (101) family of planes of hexagonal HA structure. Moreover, some irregular spherical nanocrystals could be observed in this image. These particles arise due to instability of the AV structure when exposed to electron beam irradiation, hence creating some Ag^0 nanocrystals during TEM characterization.[29,30]

In order to obtain more information about the composition and distribution of HA and AV on decorated samples, a STEM characterization was performed. For this analysis, micrographs were also recorded for the HA/AV 3 sample. In the dark-field (DF) and bright-field (BF) micrographs illustrated in Figure 4d,e, respectively, a single microrod of AV enveloped by numerous HA nanorods is observed. An elementary composition of the sample was conducted by EDS mapping of a specific region as represented by the red dashed square in Figure 4d and the magnified view in Figure 4f. In general, three main distribution profiles are observed for the elements studied. First, Ag and V elements (Figure 4g,h, respectively), which have overlapped profiles, coincide well with the main microrods observed in the BF and DF images, confirming that they consist of AV material. Second, mapping the O element (Figure 4i) gives the distribution of this element in each of the particles. Third, Ca and P elements (Figure 4j,k, respectively) also give overlapped profiles, suggesting the presence of HA

DOI: 10.1021/acs.inorgchem.9b00249
Inorg. Chem. 2019, 58, 5900−5913

nanoparticles. Moreover, their distribution is more diffuse than that of Ag and V elements and mainly appears around the microrods; i.e., they do not coincide with the regions comprised of the main microrods. Instead, an empty black region is observed where the main AV microrods are located when Ca and P mapping is performed. These results confirm that a successful synthesis of HA-decorated AV samples has been obtained.

UV−Vis Spectroscopy. In this study the optical band gap, E_g, of pure and decorated samples was estimated by extrapolating the linear portion of the UV−vis curves using the Kubelka−Munk function:[48]

$$F(R_\infty) = \frac{(1 - R_\infty)^2}{2R_\infty} = \frac{k}{s} \quad (1)$$

where $F(R_\infty)$ is the absolute reflectance of the sample, k is the molar absorption coefficient, and s is the scattering coefficient. The absorption coefficient of semiconductor oxides, α, and E_g are calculated by eq 2:[49]

$$\alpha h\nu = C_1(h\nu - E_g)^n \quad (2)$$

where α is the linear absorption coefficient of the material, $h\nu$ is the photon energy, C_1 is a proportionality constant, E_g is the optical band gap, and n is a constant associated with the different electronic transitions (n = 0.5 for direct allowed, n = 2 for indirect allowed, n = 1.5 for direct forbidden, and n = 3 for indirect forbidden). The combination of eq 1 and eq 2 gives the modified Kubelka−Munk equation:

$$[F(R_\infty)h\nu]^{1/n} = C_2(h\nu - E_g) \quad (3)$$

where $[F(R_\infty)h\nu]^{1/n}$ vs $h\nu$ was plotted to determine the E_g values of all powders. In accordance with previous studies, both HA and AV materials possess indirect allowed transitions.[50] Thus, for all the E_g estimations, we used n = 2.

Panels a−c of Figure 5 show UV−vis spectra for all studied samples. For pure HA and AV samples, E_g was found to be 5.80 and 2.65 eV, respectively, values which are consistent with the literature.[21,30] For decorated samples, the profiles are similar to those of the pure AV sample, since HA structures poorly absorb visible light. Therefore, the energy of E_g is mainly dictated by the absorption of $[VO_4]$ and $[AgO_6]$ clusters from the AV structure. A slight variation in E_g is observed in these samples, with values in the range 2.59−2.64 eV. This behavior is caused by the appearance and reorganization of intermediate levels in the forbidden zone (defective energy states) provoked by changes in structural order.[51] It should also be mentioned that although the band gaps of decorated samples are similar to those of pure AV samples, the HA energy levels are still present in decorated samples and play a crucial role in their overall electronic structure and charge distribution, as further demonstrated by the PL measurements.

Photoluminescence Emissions. Figure 6 illustrates the PL spectra recorded for the HA, AV, and HA/AV samples when excited at λ_{exc} = 350 nm at room temperature. An analysis of the results shows that the PL spectra of all samples are composed of broad-band emissions covering the visible electromagnetic spectrum in the range 350−850 nm. This kind of emission profile is typical of multilevel and multiphonon processes, where several paths involving the participation of multiple energy states within the band gap are possible during

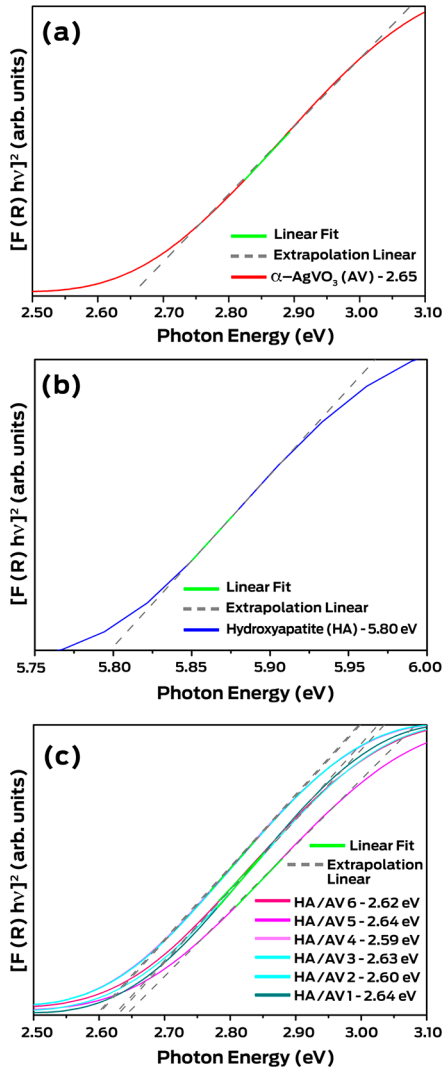

Figure 5. UV−vis spectra of pure and decorated samples at distinct molar ratios: (a) pure AV, (b) pure HA, and (c) HA-decorated AV samples.

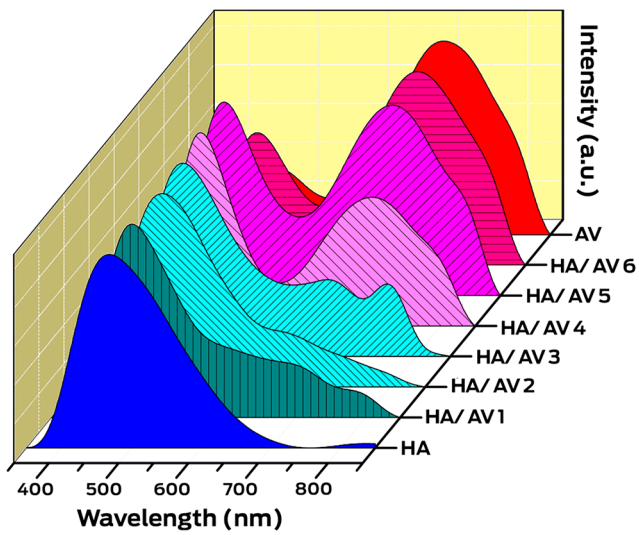

Figure 6. Tunable behavior with a red shift of the PL emissions depending on the distinct molar ratios utilized for the preparation of HA/AV samples (λ_{exc} = 350 nm).

DOI: 10.1021/acs.inorgchem.9b00249
Inorg. Chem. 2019, 58, 5900−5913

the relaxation of both HA and AV materials. The pure HA sample presents a blue emission centered at ~470 nm, which is consistent with the literature for HA obtained at low temperatures without any further treatment (e.g., heat treatments).[19,21] On the other hand, the pure α-AV sample presents two principal emission bands centered at ~460 and ~695 nm with the latter band predominant in the spectrum; this result is also consistent with the literature for this structure.[30] In a first observation, the spectra of HA/AV samples are mainly the result of superimposition of the individual HA and AV spectra, in which two maxima of intensity in the blue region (~470 nm) and another in the red region (~695 nm) are observed. The principal differences between the spectra are the relative intensities between these emission bands; i.e., a decrease in HA concentration is accompanied by a maximum displacement causing a red shift of the emission profiles (from HA/AV 1 to HA/AV 6 sample). This finding demonstrates success in obtaining tunable emission profiles in the HA-decorated AV system. From these results, we propose an order−disorder model induced by structural, surface, and interface defects to explain the PL emissions in the HA/AV system encompassing both the mixing of HA emission and AV emission as well as charge transfer mechanisms.

Figure 7 shows the Commission Internationale de l'Éclairage (CIE) chromaticity diagram for all prepared samples, and

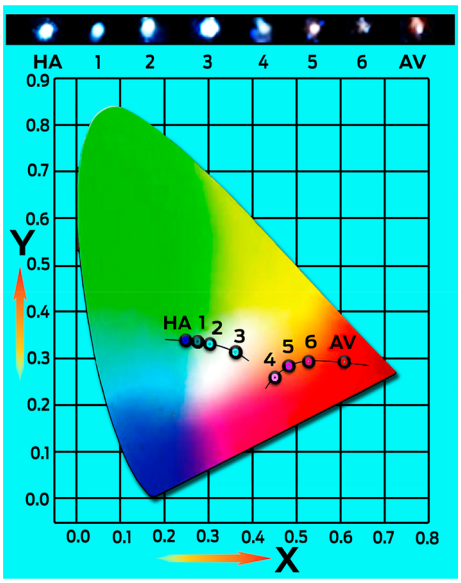

Figure 7. CIE chromaticity diagram for HA, AV, and HA/AV samples obtained at distinct molar ratios (the numbers in the graph refer to HA/AV samples from HA/AV 1 to HA/AV 6). The digital images illustrate the emitted colors during excitation of the samples at 350 nm.

Table 4 lists their corresponding x and y coordinates. Under UV excitation, the prepared samples show strong emissions, and the digital images in this figure illustrate the powders in the moment of their excitation at 350 nm. The HA and AV samples exhibit the typical bluish-white and red colors for these materials, respectively.[17,30] In HA-decorated samples, as the amount of HA decreases from HA/AV 1 to HA/AV 3, the color approximates more the central region of the CIE diagram (white region). Specifically, HA/AV 2 and HA/AV 3 samples possess CIE coordinates close to the reference values for white

Table 4. CIE Chromaticity Coordinates of All Prepared Samples

sample	x coordinate	y coordinate
HA	0.24	0.33
HA/AV 1	0.27	0.33
HA/AV 2	0.30	0.32
HA/AV 3	0.35	0.31
HA/AV 4	0.45	0.26
HA/AV 5	0.49	0.28
HA/AV 6	0.53	0.29
AV	0.61	0.29

color (x = 0.33 and y = 0.33). Hence, the emissions from HA are centered in the blue region, while the broad band of emission centered in the red region (~695 nm) of the AV structure includes emissions across much of the visible spectrum in these samples, leading to a balanced emission color with a higher white character. In samples HA/AV 4 to HA/AV 6 the decrease in the HA concentration leads to a predominant emission in the red region of the visible spectrum, which is reflected in CIE coordinates corresponding to orange and reddish emissions.

The PL emissions in the present samples are related to the participation of several energy states which are derived from bulk, surface, and interface defects of both materials. The emission spectra were deconvoluted in order to further elucidate the emission centers and to qualitatively determine the contribution of each visible light component. Figure 8 illustrates the results obtained from these deconvolutions. All profiles are well-described by the Voigt area function, and the maximum of each component remained in the same position in all samples.

The PL spectrum of pure HA in Figure 8a was deconvoluted into three components in the blue (450 nm, 2.75 eV), green (508 nm, 2.44 eV), and yellow (575 nm, 2.15 eV) regions. These emission centers have lower energies than the E_g of HA (5.80 eV). Moreover, since the excitation source used in this study also possesses lower energy than the E_g (350 nm, 3.54 eV), the defective energy levels in the forbidden zone of HA electronic structure are expected to be the main states which contribute for all the emission components observed. HA consists of a wide E_g semiconductor with significant structural flexibility (stabilization of ionic substitutions, vacancies ,and structural defects).[15] This characteristic may result in various energy states, leading to a complex electronic structure for the HA sample.

In recent years, various studies have been reported on controlling these states and manipulating them by changing the synthesis and processing conditions. Aronov et al.[52] determined in a pioneering study that electron/hole bulk and surface localized states in the band gap region are present in HA nanoceramics. Zhang et al.[17] proposed that the intense blue emission under UV light excitation of HA nano- and microcrystals might result from $CO_2^{\bullet-}$ radical impurities in the crystal lattice. Also, other carbon impurities seem to have a crucial role in the organization of energy levels of HA and electron−hole ($e'-h^{\bullet}$) radiative recombination, such as structural CO_3^{2-}, as proposed by Kumar and Girija[19] and more recently by Gonzalez et al.,[53] and carbon dots, as proposed by Jiang et al.[54] Furthermore, Bystrova et al.[55] demonstrated in a theoretical and experimental study that OH vacancies and H internodes lead to new defective energy levels

DOI: 10.1021/acs.inorgchem.9b00249
Inorg. Chem. 2019, 58, 5900−5913

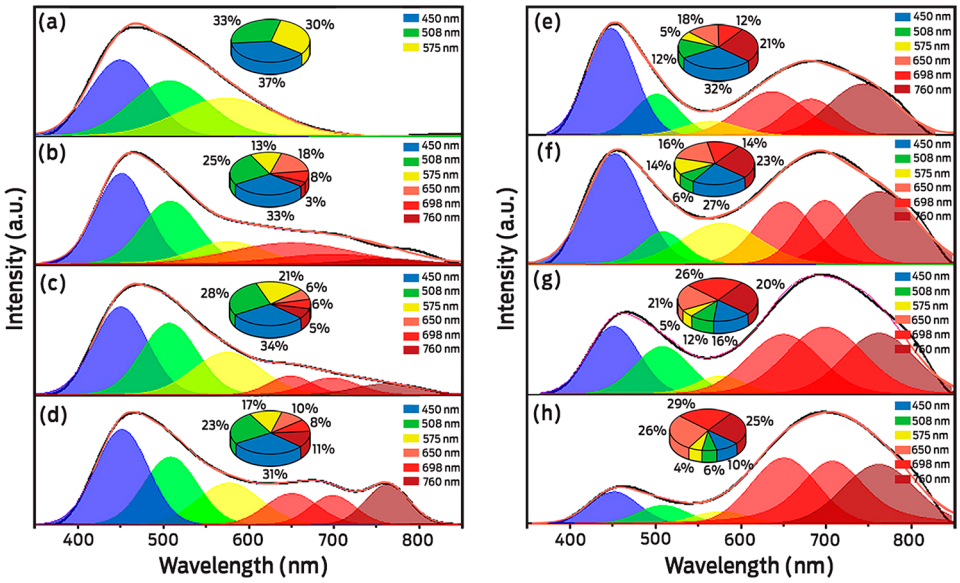

Figure 8. Deconvoluted PL spectra of HA, AV, and HA/AV samples excited at 350 nm: (a) pure HA, (b) HA/AV 1, (c) HA/AV 2, (d) HA/AV 3, (e) HA/AV 4, (f) HA/AV 5, (g) HA/AV 6, and (h) pure AV.

in the forbidden zone and can change the PL emissions of HA. Deshmukh et al.[24] reinforced the presumption of energy levels on the surface of HA particles and proposed that surface free electrons, which are confined in an asymmetric potential due to the elongated structure of HA, are optically active.

Our group studied several materials according to the broad-band model, which relates the PL emissions in semiconductors with order−disorder effects originated by the symmetry break of clusters as constituent building blocks of the material. These effects take place due to distortions of bulk and surface structure due to the presence of ionic vacancies, incorporation of impurities, and atomic displacements (deviations from ideal values of bond lengths, bond angles, and local coordination of the metals).[51,56] This loss of symmetry leads to the spontaneous formation of donor and acceptor levels within the band gap. Consequently, polarization of the lattice generates a broad-band PL profile in materials and involves radiative and nonradiative recombination of $e'-h^{\bullet}$ pairs. These energy levels within the forbidden zone can be classified as deep- or shallow-level defect states.[57] The shallow levels are more energetic, and they are responsible for violet and blue PL emissions which occur near the edge of the conduction band (CB) and/or valence band (VB). The deep levels are responsible for green, yellow, orange, and red PL emissions, and they are located near the middle of the forbidden zone.

In the case of HA, our research group,[21] by using a broad-band model, proposed that the PL emissions and organization of energy states within the band gap of HA are related to loss of symmetry in the $[CaO_9]$ and $[CaO_7H]$ clusters as well as distortions in $[PO_4]$ clusters. More broadly, this phenomenon takes place mainly by the presence of any kind of species that can decrease structural order by changing the charge distribution and symmetry of these clusters, such as Ca vacancies (ionic and interstitial), OH vacancies, protonation of the $[PO_4]$ clusters, and incorporation or further liberation (heat treatment) of impurities originating from the reactive medium (CO_3^{2-}, H_2O, NH_4^+, and $HA\cdots H^+$).[20] All of these effects provoke the generation of additional energy states into the forbidden zone associated with the Ca and P distorted clusters, including those states dominated by Ca 3p, 3d, and 4s orbitals as well as by P 3s and 3p and O 2s and 2p orbitals.[50,58,59] In the present study, the PL spectra of HA are composed of blue, green, and yellow components, indicating the contribution of both deep and shallow defective levels in the PL emissions. We believe that the PL emissions for pure HA (Figure 6 and Figure 8a) arise from the perturbation of $[CaO_9]$, $[CaO_7H]$, and $[PO_4]$ clusters at the bulk level and surface as an effect of the accommodation of CO_3^{2-} substituting PO_4 or Ca, the presence of structural H_2O, and Ca or OH vacancies, as observed by FTIR (see Figure 2). However, we cannot discard the possibility that a CO_3^{2-} impurity by itself can also contribute to the overall electronic structure of HA with additional defective energy levels to produce active PL emissions.

On the other hand, the PL spectrum of pure AV in Figure 8h presents two main broad bands and each band was deconvoluted into three components: blue (450 nm, 2.75 eV), green (508 nm, 2.44 eV), and yellow (575 nm, 2.15 eV) regions for the band centered at 460 nm, and red (650, 698, and 760 nm with corresponding energies of 1.91, 1.78, and 1.63 eV, respectively). The energy of the first component at blue is lower than the energy of the excitation source (3.54 eV) but close to the E_g value (2.64 eV), indicating that some band-to-band radiative relaxation seems to takes place in this sample. On the other hand, the other emission centers have lower energy than both E_g and the excitation source, which indicates an important contribution of defective energy levels in the forbidden zone for these PL centers of AV material. Since the AV emission spectrum is principally made up of components in the red area, it can be concluded that there is a dominant contribution of deep energy levels for the PL profile. In a recent study, De Oliveira et al.[30] demonstrated, according to the broad-band model, that the shallow defect levels originate from distortions and broken symmetry of the tetrahedral $[VO_4]$ and octahedral $[AgO_6]$ clusters and are responsible for the components of the high-energy emission band at 470 nm. On the other hand, the deep defect levels arise from oxygen vacancies leading to the three components in the red region of the electromagnetic spectrum.

DOI: 10.1021/acs.inorgchem.9b00249
Inorg. Chem. 2019, 58, 5900−5913

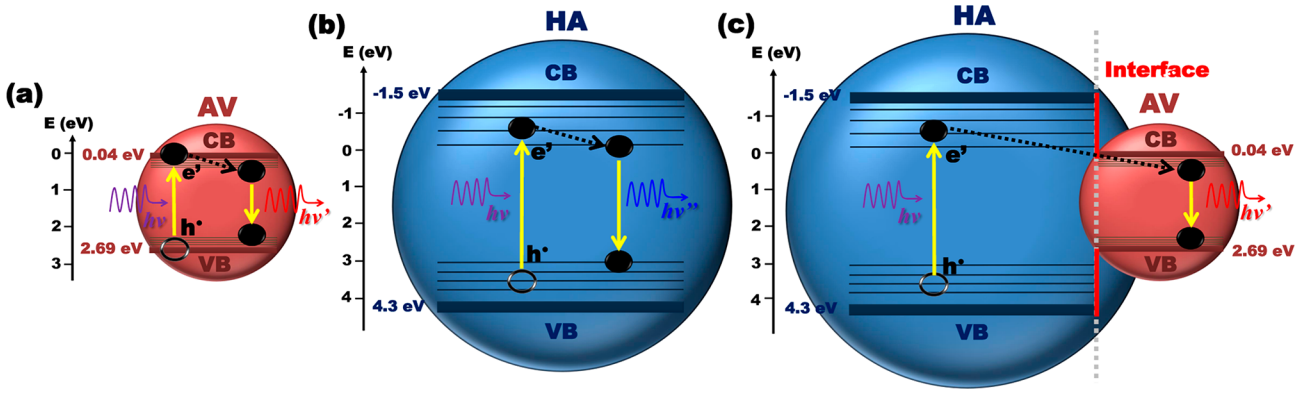

Figure 9. Proposed mechanism for PL emissions of (a) AV, (b) HA, and (c) decorated samples.

From the present results, we confirm that structural defects in HA and AV are responsible for the appearance of intermediate levels between the VB and CB, which favor PL emission at room temperature. Moreover, the synthesis of materials by soft pathways such as aqueous precipitation is known to promote general long- and short-range distortions in atomic organization (see Figure 1 and Figure 2) at the bulk level and broken bonds, stacking faults, twin boundaries, and other defects at their surfaces due to the nucleation and growth steps during the crystallization process.[60] We expect that these defects also contribute to their observed PL emissions.

Spectra of the HA-decorated AV samples show two emission bands, and six components were also needed to describe the PL profiles (three for each broad-band emission), as shown in Figure 8b−g. As expected, the area % contribution of each individual component for the PL profile follows the molar ratio between HA and AV materials; i.e., a lower concentration of HA in the HA/AV samples leads to a higher percentage of area for red components. This behavior illustrates the tunable characteristic of the emission profiles of HA/AV samples. Moreover, the most equal contributions between blue, green, yellow, and the three red components are observed in the HA/AV 3 sample, which, in turn, is reflected in a higher white character for its PL emission profile, as illustrated in Figure 8.

Interestingly, at a certain point, by decreasing the amount of HA, a decrease in the intensity of the main broad band centered at 470 nm is observed, accompanied by a relative decrease in the contribution of yellow and green components (deep levels) in comparison with the blue component (shallow levels) (see Figure 8). Hence, a valley which was not observed in the HA/AV 1 to HA/AV 3 samples is now clearly observed in the HA/AV 4 to HA/AV 6 samples. These changes in contribution from the components imply a red shift that directly affects the CIE chromaticity coordinates and emission colors of the samples (see Figure 7). Thus, it is observed that the intensities of the two main broad bands dictate the total emission color of the studied system, and the intensities of the green and yellow components play a crucial role in the transition between samples with white color emissions (HA/AV 1 to HA/AV 3) and samples with reddish color emissions (HA/AV 4 to HA/AV 6).

As in the HA and AV pure samples, the main states which dictate the profiles are associated with structural and electronic distortions of [CaO_9], [CaO_7H], and [PO_4] clusters in HA and [AgO_6] and [VO_4] in AV structures. However, in HA-decorated samples, an increase is also expected in the number of defects at the interface of the HA and AV particles. These phenomena can be directly related to the relative contributions of each individual component. Specifically, the surface contact between HA and AV particles increases with diminishing HA concentration. In the first three samples (HA/AV 1 to HA/AV 3), many HA nanoparticles are in contact with AV microrods, but some form HA agglomerates (see Figure 3). In the other samples (HA/AV 4 to HA/AV 6), practically all the HA particles are in contact with AV, forming interfaces more efficiently. Recently, our research group[21] proposed that the green and yellow components in HA spectra originate from surface and interface defects. This finding explains the present results, since a high density of interface defects could enhance nonradiative relaxation processes and partially suppress the green and yellow emissions in the HA/AV 4 to HA/AV 6 samples.

In the case of HA-decorated AV samples, charge transfer processes between the clusters from the distinct structures are also expected to take place. Hence, in order to obtain further information on the electronic structure of the studied samples, the energies associated with the edges of both CB and VB for HA and AV materials were estimated by Mulliken's theory of electronegativity:[61−63]

$$E_{CB} = X - E_C - \frac{1}{2}E_g \tag{4}$$

$$E_{VB} = E_{CB} + E_g \tag{5}$$

where X is the electronegativity of the semiconductor, which is the geometric mean of the electronegativity of the constituent atoms, E_C is the energy of free electrons of the hydrogen scale (4.50 eV); E_g is the band gap of the semiconductor; E_{CB} is the conduction band potential, and E_{VB} is the valence band potential. The electronegativity values of the AV and HA systems are 5.86 and 5.89, respectively, allowing us to determine the edge energies in accordance with the band potential calculation. Hence, the E_{VB} of AV and HA have been determined to be 2.69 and 4.29 eV, while their E_{CB} are estimated as 0.04 and −1.51 eV, respectively. On the basis of the obtained results and the pertinent literature,[21,30,50,58,59] we propose a model for the band structures of the decorated samples, as shown in Figure 9. In the case of pure AV and HA materials (Figure 9a,b, respectively), the forbidden zones exhibit several empty and occupied levels originated by defects (bulk, surface, and interface). Once the excitation radiation reaches the samples, electrons are promoted from low-energy defective states near the VB to high-energy defective states near the CB by absorbing photons ($h\nu$). There, combination

DOI: 10.1021/acs.inorgchem.9b00249
Inorg. Chem. 2019, 58, 5900−5913

between the resultant e′−h• pairs involves pathways composed of radiative and nonradiative mechanisms which allow the generation of several photons ($h\nu'$ and $h\nu''$) with energies lower than the excitation photons, leading to a broad-band PL emission.

For the HA-decorated AV samples, the radiative recombination of e′−h• pairs related to each structure separately can also take place. However, the CB edge of HA is more negative (−1.54 eV) than that of AV, whereas the VB edge of HA is much more positive (+1.60 eV) than that of AV. Hence, due to the alignment of their bands, it is also expected that other mechanisms also can produce PL emissions, in which charge transfer processes between the two materials occur because of the formation of contact interfaces. Figure 9c shows the model for HA-decorated AV samples. In this model, both the CB and VB edges of AV are located within the band gap of HA. This type of interface in heterostructures is commonly used for lasers and LEDs, and the band gap is classified as a straddling gap. The organization of bands is known to be advantageous for the charge accumulation in the material with narrower E_g (in our case, AV) and thus enhancing the e′−h• recombination process.[64] In this mechanism, the PL process takes place by the following steps: after exposure to light, the electrons excited to defective energy levels near the CB of HA nanorods are transferred to trapping levels at the AV structure, and in the following step an energetic decay process to levels near the VB of AV occurs with the liberation of photons ($h\nu'$), resulting in the PL emissions observed for decorated materials. The higher relative intensity of the band at 470 nm in relation to the band at 695 nm of the HA/AV 4 to HA/AV 6 samples in comparison to that of the pure AV sample could be related to the electrons absorbed from HA and transferred to AV by the formation of interfaces, which intensifies the radiative recombination in the blue/green region of AV. As aforementioned, the interface regions could also lead to the formation of defects which can partially trap charges for the nonradiative recombination process, reflecting in the new valley at green and yellow components in these samples.

In summary, the sum of these processes occurring between defect levels can be optimized for the preparation of materials with white-light emission. The three first samples (HA/AV 1 to HA/AV 3) do not form appropriate interfaces in which PL spectra are dominated by an equilibrium between radiative recombination in each material separately and charge transfer from HA to AV. On the other hand, samples HA/AV 4 to HA/AV 6 are capable of forming interfaces in which the charge transfer processes take place more efficiently. Considering these situations, we can discuss the possible mechanisms responsible for PL in our materials by a model based on the Kröger−Vink notation to clarify their influence on the polarization of HA/AV materials, as demonstrated by eqs 6−11:

$$2[V_{Ca}^{x}O_9] + 3[PO_4]_d^x \rightarrow [V'_{Ca}O_9] + [V''_{Ca}O_9] + 3[PO_4]^{\bullet} \quad (6)$$

$$[V_{Ca}^{x}O_7H] + [PO_4]_d^x \rightarrow [V'_{Ca}O_7H] + [PO_4]^{\bullet} \quad (7)$$

$$[CaO_9]_O^x + [PO_4]_d^x \rightarrow [CaO_9]'_O + [PO_4]_d^{\bullet} \quad (8)$$

$$[CaO_7H]_O^x + [PO_4]_d^x \rightarrow [CaO_7H]'_O + [PO_4]_d^{\bullet} \quad (9)$$

$$3[AgO_6]^x + 2[AgO_5V_O^x] \rightarrow 3[AgO_6]' + [AgO_5V_O^{\bullet}] + [AgO_5V_O^{\bullet\bullet}] \quad (10)$$

$$6[AgO_6]^x + 2[AgO_4(V_O^x)_2] \rightarrow 6[AgO_6]' + [AgO_4(V_O^{\bullet})_2] + [AgO_4(V_O^{\bullet\bullet})_2] \quad (11)$$

where eqs 6 and 7 represent the contribution of Ca vacancies in HA structure polarization, eqs 8 and 9 represent the contributions of structural defects (variations of bond lengths and angles by impurities and structural order−disorder), and eqs 10 and 11 represent the polarization caused by oxygen vacancies in the AV structure. In HA and HA/AV 1 samples, there is a predominance of structural defects from HA for PL emissions and the clusters from eqs 6 and 7 do not undergo charge exchange with clusters from eqs 8 and 9. At equilibrium (samples HA/AV 2 and HA/AV 3) there is a formation of e′−h• pairs with trapping occurring in clusters from eqs 6 to 9 in HA as well as clusters from eqs 10 and 11 of AV. Charge exchange between them and the shallow defects from order−disorder effects in AV are also feasible. Finally, at low concentrations of HA, there exists a predominance of oxygen defects from AV from eqs 10 and 11 for PL emissions.

Hence, the changes observed in the intensity and shape of the PL emissions in decorated materials could be associated with the variations of molar ratios between HA and AV, which directly affect the contribution of each mechanism (radiative recombination between each material or charge transfer, and interface defects) for the final emission profile. The most common strategy to obtain white-light emission is the mixing of three monochromatic sources (red, green, and blue) departing from electronic transitions of lanthanide elements.[2] In this study, we propose a strategy to produce white-light emission by broad-band emissions from defective energy levels of complex semiconductors without the necessity of dopants. We show here that the HA/AV 2 and HA/AV 3 samples exhibit balanced contributions over the entire visible range of the electromagnetic spectrum with components well-distributed in the blue, green, yellow, and red regions, generating white emissions. Another important fact is the format of the continuous emission profile corresponding to the HA/AV 3 sample, which is similar to the daylight spectrum.[65] Hence, by avoiding the discontinuity of the emission profile in this sample, some benefits arise for possible applications of HA/AV systems, such as an accurate emulation of natural daylight color or incandescent light on digital screens.[66] The method proposed here, by combining two semiconductors, exhibits intense self-activated PL emissions and opens the door for obtaining tunable emissions and white light from materials.

Bactericidal Activity of the HA/AV System. In this study, in order to also demonstrate the potential of the HA/AV system as a novel bactericidal material, the antimicrobial activity of pure HA and AV samples, as well as two representative HA/AV decorated compounds (HA/AV 1 and HA/AV 6) were tested against two standard strains of *S. aureus*, one resistant (MRSA) and one susceptible to methicillin (MSSA). The most important difference between MRSA and MSSA cells is sensitivity to β-lactam antibiotics. MRSA strains are resistant to all antibiotics of this type and are prone to resistance to other antibiotics more easily than MSSA.[67] Concern about fighting against super-resistant bacteria drives the need to develop new materials. Table 5

DOI: 10.1021/acs.inorgchem.9b00249
Inorg. Chem. 2019, 58, 5900−5913

Table 5. Response to Treatment with HA, AV, and HA/AV in CFU/mL in the MRSA and MSSA Bacteria for 24 h

	MIC (μg/mL)	
sample	MRSA	MSSA
HA	not found	not found
HA/AV 1	1000	1000
HA/AV 6	250	250
AV	125	125

summarizes the CFU/mL of the MRSA and MSSA bacteria after a 24 h treatment with pure and decorated materials. Samples with a higher proportion of AV in the HA/AV system caused an overall higher bactericidal activity for decorated samples.

It is known that AV exhibits high bactericidal activity, including against resistant bacteria.[30] It can be seen that HA without AV showed no bactericidal activity. This observation is in accordance with the literature, since Ag incorporation in the HA lattice or surface is necessary to induce bactericidal activity in HA material for reduction of implant-related infections.[68] The decoration of HA with other Ag-based materials, such as Ag_3PO_4 and Ag nanoparticles,[69,70] is also a strategy reported elsewhere. HA-decorated AV samples have an improved ability to inhibit both MRSA and MSSA bacteria, and no significant differences were observed between their activities. The AV structure when associated with HA gives the overall system the ability to release ROS when in contact with the bacteria. These reactive species are responsible for damage to the membranes of microorganisms, leading to their elimination.[30,71]

In order to evaluate the ROS production of the materials, probes along the photocatalytic activity were performed with the addition of appropriate scavengers for the reactive species (see Figure S3 in the Supporting Information). We selected HA, AV, and HA/AV 6 as the representative samples for the probes. In pure HA, $O_2^{\bullet-}$ radical is the major species generated since there is a decrease in RhB photodegradation with the addition of AA, followed by $OH^\bullet$ (TBA) and, less importantly, $h^\bullet$ (AO); for pure AV, the three $O_2^{\bullet-}$, $OH^\bullet$, and $h^\bullet$ species are similarly sensed. On the other hand, in the decorated sample (HA/AV 6), there is a principal influence of $O_2^{\bullet-}$ on RhB photodegradation, indicating that this is the major species present, followed by $h^\bullet$. Also, a high suppression of $OH^\bullet$ generation is observed for the HA/AV 6 sample.

In summary, based on the above results, the $O_2^{\bullet-}$ species can be considered as the key ROS for the bactericidal activity of the HA/AV 6 sample. The high suppression of $OH^\bullet$ radicals in comparison with those of the pure HA and AV samples is probably because of synergetic effects by their association. This synergetic effect is also evidenced by the increase in the photodegradation capacity of the HA/AV 6 sample to RhB (94%) in comparison to thos of pure samples (35% and 29% for HA and AV samples, respectively). Hence, the association between HA and AV materials shows the potential to obtain systems with promising optical and antibacterial properties.

CONCLUSIONS

In this work, AV microrods were decorated with nanorods of HA by chemical precipitation. These composites were synthesized at different HA/AV molar ratios, allowing the emission of a wide range of colors between the blue of HA and the red of AV, obeying a trend observed in the CIE chromaticity diagram, including two samples with bluish white-light emissions. It was demonstrated that bulk, surface, and interface defects, as well as charge transfer mechanisms between HA and AV materials, play crucial roles in their optical properties. This strategy to tune photoluminescence emissions is extremely powerful for obtaining LEDs of different colors and also creates the possibility of tuning photoluminescence emissions to any desired application. Another interesting fact caused by the combination of these two materials is the simple and efficient production of samples with improved bactericidal properties, for potential applications where biocompatible systems are needed. In this way, we have in hand a multifunctional material with promising optical and biomedical applications.

ASSOCIATED CONTENT

Supporting Information

The Supporting Information is available free of charge on the ACS Publications website at DOI: 10.1021/acs.inorgchem.9b00249.

Full FTIR spectra for all samples; RAMAN spectra as well as tables indicating the vibrational modes assigned; plots of reactive species evaluated by RhB photocatalytic degradation (PDF)

AUTHOR INFORMATION

Corresponding Author

*E-mail: elson.liec@gmail.com.

ORCID

Thales R. Machado: 0000-0002-3246-6329
Marcelo Assis: 0000-0003-0355-5565
Camila C. Foggi: 0000-0002-1210-1234
Nadia G. Macedo: 0000-0001-7031-2729
Héctor Beltrán-Mir: 0000-0002-7836-1602
Juan Andrés: 0000-0003-0232-3957
Elson Longo: 0000-0001-8062-7791

Notes

The authors declare no competing financial interest.

ACKNOWLEDGMENTS

We acknowledge the financial support of following agencies: Coordenação de Aperfeiçoamento de Pessoal de Nível Superior—Brazil (CAPES), Financial Code 001; the PNPD Program; FAPESP (Grant 2013/07296-2); and CNPq (Grants 141964/2018-9 and 133661/2016-4). J.A. acknowledges financial support from Universitat Jaume I, Project UJI-B2016-25; Generalitat Valenciana Project Prometeo/2016/079; and Ministerio de Economia y Competitividad, Project CTQ2015-65207-P. Special thanks to Enio Longo for design contributions and Rorivaldo Carmago for TEM operation.

REFERENCES

(1) Xia, Z.; Liu, Q. Progress in Discovery and Structural Design of Color Conversion Phosphors for LEDs. *Prog. Mater. Sci.* **2016**, *84*, 59−117.

(2) Smet, P. F.; Parmentier, A. B.; Poelman, D. Selecting Conversion Phosphors for White Light-Emitting Diodes. *J. Electrochem. Soc.* **2011**, *158*, R37−R54.

(3) Neupane, J.; Ghimire, S.; Shakya, S.; Chaudhary, L.; Shrivastava, V. P. Effect of Light Emitting Diodes in the Photodynamic Therapy of Rheumatoid Arthritis. *Photodiagn. Photodyn. Ther.* **2010**, *7*, 44−49.

(4) Lerche, C. M.; Heerfordt, I. M.; Heydenreich, J.; Wulf, H. C. Alternatives to Outdoor Daylight Illumination for Photodynamic

DOI: 10.1021/acs.inorgchem.9b00249
Inorg. Chem. 2019, 58, 5900−5913

Therapy - use of Greenhouses and Artificial Light Sources. *Int. J. Mol. Sci.* **2016**, *17*, 309.
(5) Chen, L.; Lin, C. C.; Yeh, C. W.; Liu, R. S. Light Converting Inorganic Phosphors for White Light-Emitting Diodes. *Materials* **2010**, *3*, 2172−2195.
(6) Xie, F.; Zhang, T. A.; Dreisinger, D.; Doyle, F. A Critical Review on Solvent Extraction of Rare Earths from Aqueous Solutions. *Miner. Eng.* **2014**, *56*, 10−28.
(7) Shang, M.; Li, C.; Lin, J. How to Produce White Light in a Single-Phase Host? *Chem. Soc. Rev.* **2014**, *43*, 1372−1386.
(8) Zhang, C.; Lin, J. Defect-Related Luminescent Materials: Synthesis, Emission Properties and Applications. *Chem. Soc. Rev.* **2012**, *41*, 7938−7961.
(9) Jakob, A. M.; Schmedake, T. A. A Novel Approach to Monodisperse, Luminescent Silica Spheres. *Chem. Mater.* **2006**, *18*, 3173−3175.
(10) Zhang, C.; Li, C.; Yang, J.; Cheng, Z.; Hou, Z.; Fan, Y.; Lin, J. Tunable Luminescence in Monodisperse Zirconia Spheres. *Langmuir* **2009**, *25*, 7078−7083.
(11) Gupta, S. K.; Ghosh, P. S.; Pathak, N.; Tewari, R. Nature of Defects in Blue Light Emitting $CaZrO_3$: Spectroscopic and Theoretical Study. *RSC Adv.* **2015**, *5*, 56526−56533.
(12) Ogi, T.; Kaihatsu, Y.; Iskandar, F.; Wang, W. N.; Okuyama, K. Facile Synthesis of New Full-Color-Emitting BCNO Phosphors with High Quantum Efficiency. *Adv. Mater.* **2008**, *20*, 3235−3238.
(13) Ge, K.; Zhang, C.; Jia, G.; Ren, H.; Wang, J.; Tan, A.; Liang, X. J.; Zang, A.; Zhang, J. Defect-Related Luminescent Mesoporous Silica Nanoparticles Employed for Novel Detectable Nanocarrier. *ACS Appl. Mater. Interfaces* **2015**, *7*, 10905−10914.
(14) Vallet-Regí, M.; González-Calbet, J. M. Calcium Phosphates as Substitution of Bone Tissues. *Prog. Solid State Chem.* **2004**, *32*, 1−31.
(15) Uskoković, V. The Role of Hydroxyl Channel in Defining Selected Physicochemical Peculiarities Exhibited by Hydroxyapatite. *RSC Adv.* **2015**, *5*, 36614−36633.
(16) Wopenka, B.; Pasteris, J. D. A Mineralogical Perspective on the Apatite in Bone. *Mater. Sci. Eng., C* **2005**, *25*, 131−143.
(17) Zhang, C.; Yang, J.; Quan, Z.; Yang, P.; Li, C.; Hou, Z.; Lin, J. Hydroxyapatite Nano- and Microcrystals with Multiform Morphologies: Controllable Synthesis and Luminescence Properties. *Cryst. Growth Des.* **2009**, *9*, 2725−2733.
(18) Zhang, C.; Huang, S.; Yang, D.; Kang, X.; Shang, M.; Peng, C.; Lin, J. Tunable Luminescence in Ce^{3+}, Mn^{2+}-Codoped Calcium Fluorapatite through Combining Emissions and Modulation of Excitation: A Novel Strategy to White Light Emission. *J. Mater. Chem.* **2010**, *20*, 6674−6680.
(19) Kumar, G. S.; Girija, E. K. Flower-like Hydroxyapatite Nanostructure Obtained from Eggshell: A Candidate for Biomedical Applications. *Ceram. Int.* **2013**, *39*, 8293−8299.
(20) Machado, T. R.; Sczancoski, J. C.; Beltrán-Mir, H.; Nogueira, I. C.; Li, M. S.; Andrés, J.; Cordoncillo, E.; Longo, E. A Novel Approach to Obtain Highly Intense Self-Activated Photoluminescence Emissions in Hydroxyapatite Nanoparticles. *J. Solid State Chem.* **2017**, *249*, 64−69.
(21) Machado, T. R.; Sczancoski, J. C.; Beltrán-Mir, H.; Li, M. S.; Andrés, J.; Cordoncillo, E.; Leite, E.; Longo, E. Structural Properties and Self-Activated Photoluminescence Emissions in Hydroxyapatite with Distinct Particle Shapes. *Ceram. Int.* **2018**, *44*, 236−245.
(22) Zhang, C.; Li, C.; Huang, S.; Hou, Z.; Cheng, Z.; Yang, P.; Peng, C.; Lin, J. Self-Activated Luminescent and Mesoporous Strontium Hydroxyapatite Nanorods for Drug Delivery. *Biomaterials* **2010**, *31*, 3374−3383.
(23) Singh, R. K.; Kim, T. H.; Patel, K. D.; Kim, J. J.; Kim, H. W. Development of Biocompatible Apatite Nanorod-Based Drug-Delivery System with in Situ Fluorescence Imaging Capacity. *J. Mater. Chem. B* **2014**, *2*, 2039−2050.
(24) Deshmukh, K.; Shaik, M. M.; Ramanan, S. R.; Kowshik, M. Self-Activated Fluorescent Hydroxyapatite Nanoparticles: A Promising Agent for Bioimaging and Biolabeling. *ACS Biomater. Sci. Eng.* **2016**, *2*, 1257−1264.
(25) Park, S. Y.; Kim, K. Il; Park, S. P.; Lee, J. H.; Jung, H. S. Aspartic Acid-Assisted Synthesis of Multifunctional Strontium-Substituted Hydroxyapatite Microspheres. *Cryst. Growth Des.* **2016**, *16*, 4318−4326.
(26) Wang, C.; Liu, D.; Zhang, C.; Sun, J.; Feng, W.; Liang, X. J.; Wang, S.; Zhang, J. Defect-Related Luminescent Hydroxyapatite-Enhanced Osteogenic Differentiation of Bone Mesenchymal Stem Cells Via an ATP-Induced cAMP/PKA Pathway. *ACS Appl. Mater. Interfaces* **2016**, *8*, 11262−11271.
(27) McNulty, D.; Ramasse, Q.; O'Dwyer, C. The Structural Conversion from α-$AgVO_3$ to β-$AgVO_3$: Ag Nanoparticle Decorated Nanowires with Application as Cathode Materials for Li-Ion Batteries. *Nanoscale* **2016**, *8*, 16266−16275.
(28) Tracey, A. S.; Willsky, G. R.; Takeuchi, E. S. *Vanadium: Chemistry, Biochemistry, Pharmacology and Practical Applications*; CRC Press: Boca Raton, FL, USA, 2007.
(29) De Oliveira, R. C.; Assis, M.; Teixeira, M. M.; Da Silva, M. D. P.; Li, M. S.; Andres, J.; Gracia, L.; Longo, E. An Experimental and Computational Study of β-$AgVO_3$: Optical Properties and Formation of Ag Nanoparticles. *J. Phys. Chem. C* **2016**, *120*, 12254−12264.
(30) De Oliveira, R. C.; De Foggi, C. C.; Teixeira, M. M.; Da Silva, M. D. P.; Assis, M.; Francisco, E. M.; Pimentel, B. N. A. D. S.; Pereira, P. F. D. S.; Vergani, C. E.; Machado, A. L.; et al. Mechanism of Antibacterial Activity via Morphology Change of α-$AgVO_3$: Theoretical and Experimental Insights. *ACS Appl. Mater. Interfaces* **2017**, *9*, 11472−11481.
(31) Kittaka, S.; Nishida, S.; Iwashita, T.; Ohtani, T. Reactivity and Structural Properties of a Mechanochemically Treated Ag_2O-V_2O_5 system in Relation to $AgVO_3$ polymorphs. *J. Solid State Chem.* **2002**, *164*, 144−149.
(32) Kittaka, S.; Matsuno, K.; Akashi, H. Crystal Structure of α-$AgVO_3$ and Phase Relation of $AgVO_3$. *J. Solid State Chem.* **1999**, *142*, 360−367.
(33) Oliveira, R. C.; Teixeira, M. M.; Costa, J. P. C.; Penha, M.; Francisco, E. M.; da Silva, J. S.; Li, M. S.; Longo, E.; Gracia, L.; Andrés, J. α- and β-$AgVO_3$ Polymorphs as Photoluminescent Materials: An Example of Temperature-Driven Synthesis. *Ceram. Int.* **2018**, *44*, 5939−5944.
(34) Liu, H.; Feng, Y.; Chen, D.; Li, C.; Cui, P.; Yang, J. Noble Metal-Based Composite Nanomaterials Fabricated via Solution-Based Approaches. *J. Mater. Chem. A* **2015**, *3*, 3182−3223.
(35) Mondego, M.; de Oliveira, R. C.; Penha, M.; Li, M. S.; Longo, E. Blue and Red Light Photoluminescence Emission at Room Temperature from $CaTiO_3$ decorated with α-Ag_2WO_4. *Ceram. Int.* **2017**, *43*, 5759−5766.
(36) Amoresi, R. A. C.; Teodoro, V.; Teixeira, G. F.; Li, M. S.; Simões, A. Z.; Perazolli, L. A.; Longo, E.; Zaghete, M. A. Electrosteric Colloidal Stabilization for Obtaining $SrTiO_3/TiO_2$ heterojunction: Microstructural Evolution in the Interface and Photonics Properties. *J. Eur. Ceram. Soc.* **2018**, *38*, 1621−1631.
(37) *Labsphere webpage*; http://www.labsphere.com (accessed Sep. 7, 2018).
(38) Sudarsanan, K.; Young, R. A. Significant Precision in Crystal Structural Details. Holly Springs Hydroxyapatite. *Acta Crystallogr., Sect. B: Struct. Crystallogr. Cryst. Chem.* **1969**, *25*, 1534−1543.
(39) Zyman, Z. Z.; Rokhmistrov, D. V.; Glushko, V. I.; Ivanov, I. G. Thermal Impurity Reactions and Structural Changes in Slightly Carbonated Hydroxyapatite. *J. Mater. Sci.: Mater. Med.* **2009**, *20*, 1389−1399.
(40) Fowler, B. O. Infrared Studies of Apatites. I. Vibrational Assignments for Calcium, Strontium, and Barium Hydroxyapatites Utilizing Isotopic Substitution. *Inorg. Chem.* **1974**, *13*, 194−207.
(41) Marković, S.; Veselinović, L.; Lukić, M. J.; Karanović, L.; Bračko, I.; Ignjatović, N.; Uskoković, D. Synthetical Bone-like and Biological Hydroxyapatites: A Comparative Study of Crystal Structure and Morphology. *Biomed. Mater.* **2011**, *6*, No. 045005.
(42) Fleet, M. *Carbonated hydroxyapatite: Materials, Synthesis, and Applications*; Pan Stanford: New York, 2015.

DOI: 10.1021/acs.inorgchem.9b00249
Inorg. Chem. 2019, 58, 5900−5913

(43) Elliot, J.C. *Structure and Chemistry of the Apatites and Other Calcium Orthophosphates*, Vol. *18*; Elsevier: Amsterdam, 1994.
(44) Sivakumar, V.; Suresh, R.; Giribabu, K.; Narayanan, V. $AgVO_3$ Nanorods: Synthesis, Characterization and Visible Light Photocatalytic Activity. *Solid State Sci.* **2015**, *39*, 34−39.
(45) Andronache, C. I.; Racolta, D. Structural Investigation of MO·P_2O_5·Li_2O (MO = Fe_2O_3 or V_2O_5) Glass Systems by FTIR Spectroscopy. *AIP Conf. Proc.* **2013**, *1634*, 115−119.
(46) Holtz, R. D.; Souza Filho, A. G.; Brocchi, M.; Martins, D.; Durán, N.; Alves, O. L. Development of Nanostructured Silver Vanadates Decorated with Silver Nanoparticles as a Novel Antibacterial Agent. *Nanotechnology* **2010**, *21*, 185102.
(47) Antonakos, A.; Liarokapis, E.; Leventouri, T. Micro-Raman and FTIR Studies of Synthetic and Natural Apatites. *Biomaterials* **2007**, *28*, 3043−3054.
(48) Kubelka, P.; Munk, F. Ein Beitrag zur Optik der Farbanstriche. *Z. Tech. Phys.* **1931**, *12*, 593−601.
(49) Wood, D. L.; Tauc, J. Weak Absorption Tails in Amorphous Semiconductors. *Phys. Rev. B* **1972**, *5*, 3144−3151.
(50) Slepko, A.; Demkov, A. A. First-Principles Study of the Biomineral Hydroxyapatite. *Phys. Rev. B: Condens. Matter Mater. Phys.* **2011**, *84*, 134108.
(51) Gouveia, A. F.; Sczancoski, J. C.; Ferrer, M. M.; Lima, A. S.; Santos, M. R. M. C.; Li, M. S.; Santos, R. S.; Longo, E.; Cavalcante, L. S. Experimental and Theoretical Investigations of Electronic Structure and Photoluminescence Properties of β-Ag_2MoO_4 Microcrystals. *Inorg. Chem.* **2014**, *53*, 5589−5599.
(52) Aronov, D.; Karlov, A.; Rosenman, G. Hydroxyapatite Nanoceramics: Basic Physical Properties and Biointerface Modification. *J. Eur. Ceram. Soc.* **2007**, *27*, 4181−4186.
(53) Gonzalez, G.; Costa-Vera, C.; Borrero, L. J.; Soto, D.; Lozada, L.; Chango, J. I.; Diaz, J. C.; Lascano, L. Effect of Carbonates on Hydroxyapatite Self-Activated Photoluminescence Response. *J. Lumin.* **2018**, *195*, 385−395.
(54) Jiang, D.; Zhao, H.; Yang, Y.; Zhu, Y.; Chen, X.; Sun, J.; Yu, K.; Fan, H.; Zhang, X. Investigation of Luminescent Mechanism: N-Rich Carbon Dots as Luminescence Centers in Fluorescent Hydroxyapatite Prepared Using a Typical Hydrothermal Process. *J. Mater. Chem. B* **2017**, *5*, 3749−3757.
(55) Bystrova, A. V.; Dekhtyar, Y. D.; Popov, A. I.; Coutinho, J.; Bystrov, V. S. Modeling and Synchrotron Data Analysis of Modified Hydroxyapatite Structure. *Ferroelectrics* **2015**, *475*, 135−147.
(56) Anicete-Santos, M.; Orhan, E.; De Maurera, M. A. M. A.; Simões, L. G. P.; Souza, A. G.; Pizani, P. S.; Leite, E. R.; Varela, J. A.; Andrés, J.; Beltrán, A.; Longo, E. Contribution of Structural Order-Disorder to the Green Photoluminescence of $PbWO_4$. *Phys. Rev. B: Condens. Matter Mater. Phys.* **2007**, *75*, 165105.
(57) McCluskey, M. D.; Haller, E. E. *Dopants and Defects in Semiconductors*; Taylor & Francis: London, 2012.
(58) Matsunaga, K.; Kuwabara, A. First-Principles Study of Vacancy Formation in Hydroxyapatite. *Phys. Rev. B: Condens. Matter Mater. Phys.* **2007**, *75*, 014102.
(59) Bystrov, V. S.; Coutinho, J.; Bystrova, A. V.; Dekhtyar, Y. D.; Pullar, R. C.; Poronin, A.; Palcevskis, E.; Dindune, A.; Alkan, B.; Durucan, C.; et al. Computational Study of Hydroxyapatite Structures, Properties and Defects. *J. Phys. D: Appl. Phys.* **2015**, *48*, 195302.
(60) Haranath, D.; Shanker, V.; Vij, D. R. *Handbook of Electroluminescent Materials*; Taylor & Francis: London, 2004.
(61) Mulliken, R. S. A New Electroaffinity Scale; Together with Data on Valence States and on Valence Ionization Potentials and Electron Affinities. *J. Chem. Phys.* **1934**, *2*, 782−793.
(62) Walsh, A.; Butler, K. T. Prediction of Electron Energies in Metal Oxides. *Acc. Chem. Res.* **2014**, *47*, 364−372.
(63) Wang, X.; Wan, X.; Xu, X.; Chen, X. Facile Fabrication of Highly Efficient AgI/ZnO Heterojunction and Its Applications of Methylene Blue and Rhodamine B Solutions Degradation under Natural Sunlight. *Appl. Surf. Sci.* **2014**, *321*, 10−18.
(64) Li, X.; Xu, P.; Chen, M.; Zeng, G.; Wang, D.; Chen, F.; Tang, W.; Chen, C.; Zhang, C.; Tan, X. Application of Silver Phosphate-Based Photocatalysts: Barriers and Solutions. *Chem. Eng. J.* **2019**, *366*, 339−357.
(65) Xu, T.; Li, W.; Gao, X.; Sun, C.; Chen, G.; Zhang, X.; Li, C.; Zhu, W.; Wei, B. Temperature and Exciton Concentration Induced Excimer Emission of 4,4'-Bis(4"Triphenylsilyl) Phenyl-1,1'-Binaphthalene and Application for Sunlight-Like White Organic Light-Emitting Diodes. *Nanoscale Res. Lett.* **2016**, *11*, 379.
(66) Houser, K.; Mossman, M.; Smet, K.; Whitehead, L. Tutorial: Color Rendering and Its Applications in Lighting. *Leukos* **2016**, *12*, 7−26.
(67) Rozgonyi, F.; Kocsis, E.; Kristóf, K.; Nagy, K. Is MRSA More Virulent than MSSA? *Clin. Microbiol. Infect.* **2007**, *13*, 843−845.
(68) Lim, P. N.; Chang, L.; Thian, E. S. Development of Nanosized Silver-Substituted Apatite for Biomedical Applications: A Review. *Nanomedicine* **2015**, *11*, 1331−1344.
(69) Li, Y.; Zhou, H.; Zhu, G.; Shao, C.; Pan, H.; Xu, X.; Tang, R. High Efficient Multifunctional Ag_3PO_4 Loaded Hydroxyapatite Nanowires for Water Treatment. *J. Hazard. Mater.* **2015**, *299*, 379−387.
(70) Xiong, Z. C.; Zhu, Y. J.; Chen, F. F.; Sun, T. W.; Shen, Y. Q. One-Step Synthesis of Silver Nanoparticle-Decorated Hydroxyapatite Nanowires for the Construction of Highly Flexible Free-Standing Paper with High Antibacterial Activity. *Chem. - Eur. J.* **2016**, *22*, 11093.
(71) Chen, Z.; Wang, Z.; Ren, J.; Qu, X. Enzyme Mimicry for Combating Bacteria and Biofilms. *Acc. Chem. Res.* **2018**, *51*, 789−799.

DOI: 10.1021/acs.inorgchem.9b00249
Inorg. Chem. 2019, 58, 5900−5913